Computational Modeling of Jet Vanes for Thrust Vector Control

Hector Sanchez*, Sameer Sheth†, Rushil Negandhi‡, Jackson Meyers§
Georgia Institute of Technology, Atlanta, Georgia, 30332,

In rocketry, thrust vector control (TVC) guides a vehicle's thrust to perform controlled maneuvers. In particular, jet vane TVC (JVTVC) performs thrust vectoring and active stabilization through the actuation of diamond-shaped control surfaces placed in the exhaust. The Guidance, Navigation, and Control (GNC) team at Georgia Institute of Technology's Ramblin' Rocket Club aims to develop a JVTVC system for a solid-propellant rocket. To characterize jet vane performance, computational fluid dynamics (CFD) analyses were conducted for deflection angles ranging from 0 to 30 degrees and chamber pressures ranging from 1 to 4 MPa. Ansys Fluent was used to generate unstructured meshes and perform simulations with the density-based solver and the k-ω SST turbulence model. Furthermore, conjugate heat transfer (CHT) analysis of the jet vane and vane backing was conducted using a fluid-solid coupled mesh. The CHT analysis utilized a method that decreased the computational cost of the simulation. Finally, this CFD study produced regression models as functions of the deflection angle and thrust for the vane side force and drag whose results can be used in flight control simulations. The methodology of this study can inform medium-fidelity three-dimensional CFD analysis of jet vanes for actively stabilized rocketry at the collegiate level.

I. Nomenclature

A	=	Area, m^2
A^*	=	Throat area, m^2
$[B, C, D, E]$	=	Regression Model Coefficients
F_T	=	Thrust, N
F_{T_R}	=	Thrust Reduction, N
F_S	=	Side Force, N
k	=	Turbulent kinetic energy, m^2/s^2
M	=	Mach number
$\dot{m}$	=	Mass flow rate, kg/s
p	=	Static pressure, Pa
p_a	=	Ambient pressure, Pa
p_e	=	Exit static pressure, Pa
p_0	=	Stagnation pressure, Pa
R	=	Specific gas constant, J/(kg· K)
T	=	Static temperature, K
T_0	=	Stagnation temperature, K
v	=	Velocity, m/s
v_e	=	Exit velocity, m/s
$y+$	=	Non-dimensionalized distance from wall for turbulence modeling
α	=	Deflection Angle, degrees
γ	=	Specific heat ratio
ϵ	=	Turbulence dissipation rate, m^2/s^3
ω	=	Specific turbulence dissipation rate, 1/s

*Undergraduate Member, GT Ramblin' Rocket Club, Daniel Guggenheim School of Aerospace Engineering, AIAA Student Member 1419750
†Undergraduate Member, GT Ramblin' Rocket Club, Daniel Guggenheim School of Aerospace Engineering, AIAA Student Member, 1603262
‡Undergraduate Member, GT Ramblin' Rocket Club, Daniel Guggenheim School of Aerospace Engineering, AIAA Student Member, 1406070
§Undergraduate Member, GT Ramblin' Rocket Club, Daniel Guggenheim School of Aerospace Engineering, AIAA Student Member, 1809877

II. Introduction

Thrust vector control (TVC) is a critical technology in large-scale rocketry, enabling vehicles to actively steer and stabilize during flight. By deflecting the engine exhaust, the TVC system generates a side force about the center of gravity that allows a rocket to maintain or change its trajectory. Active control and stabilization through control surfaces, such as canards, are also viable options. However, these control surfaces become less effective at low velocities or high altitudes, where the aerodynamic control authority is decreased, compared to active control through TVC, allowing for higher control authority over the entire powered flight profile [1]. As a result, this is a valuable capability for launch vehicles, sounding rockets, and guided projectiles, which may need high control authority at take off and higher speeds in the upper atmosphere.

There are three primary types of methods for TVC. The most common type involves using a movable nozzle, however, only control in the pitch and yaw axis is enabled through these methods. Roll control requires forces to be exerted about the roll axis, which is impossible if solely changing the orientation of a single nozzle. The other two types of TVC involve injecting a secondary fluid or obstructing the flow [1, 2]. This paper focuses on jet vane thrust vector control (JVTVC), which falls under the latter type of methods. JVTVC utilizes small, fin-shaped deflectors placed just aft of the nozzle exit plane, where the deflectors are capable of altering the direction of the rocket exhaust. Jet vanes are designed to have sharp edges that cause an oblique shock on the front end and an expansion fan on the rear end, allowing the jet vanes to generate lift with a deflection angle similar to a supersonic wing at an angle of attack. Furthermore, since the vanes are offset from the roll axis, these small lifting forces are also capable of controlling roll during flight [3]. Mechanically, jet vanes offer a relatively simple solution compared to gimbaled nozzles and fluid injection. A gimbaled nozzle is difficult to use with solid rocket motors due to ablation and erosion of the nozzle, and fluid injection typically requires the use of a separate liquid tank [4, 5].

The Guidance, Navigation, and Control (GNC) team under the Georgia Institute of Technology's Ramblin' Rocket Club aims to develop a JVTVC system for a solid-propellant rocket as part of an effort to launch a high-powered actively stabilized rocket. Designing and operating a jet vanes system requires thorough understanding of their aerodynamic performance, such as the lift and drag produced by the vanes. [3, 6]. Computational fluid dynamics (CFD) can be used to evaluate jet vane performance, which involves numerically solving the governing equations of fluid flow. Additionally, CFD simulations can directly determine the side force, or lift, produced by the vane, the total thrust reduction, and the heat transfer through the JVTVC assembly.

This study presents a medium-fidelity CFD analysis of jet vanes to characterize their performance. Using the commercial CFD software Ansys Fluent, simulations were conducted to capture the complex flow structures due to the jet vanes and nozzle exhaust. The vanes were simulated at deflection angles of 0°, 10°, 20°, and 30° with six different input pressure conditions to reflect the varying thrust of the solid rocket motor. Furthermore, transient conjugate heat transfer (CHT) analysis was performed to evaluate and understand the thermal conditions being applied to the jet vanes.

The findings of this study can inform the design and implementation of JVTVC systems for collegiate-level rocketry. By developing regression models of the vane side force and thrust reduction as functions of the deflection angle and thrust applied, this study provided a foundation for the development of GNC's flight controller. Furthermore, the procedure employed can serve as a reference for others who are also engaged in high-power rocketry projects and require efficient performance predictions for jet vane and other TVC-based control architectures.

III. Computational Geometry

The computational geometry used in these studies is based on the complete assembly of GNC's JVTVC system and the exhaust of an AeroTech N1000W-PS solid rocket motor with a Rocket Motor Components (RCS) 98 mm nozzle. The JVTVC system is designed around a series of components that allow servo motors to deflect the jet vanes in the motor's exhaust, changing the direction of the thrust vector. These deflections occur about the midpoint of a vane as they are held in place by vane backings connected to a servo with an axle and gear system. The angle between the vane's center line and the horizontal component of the motor's exhaust is the deflection angle as shown in Fig. 1.

The vanes were designed around a double-wedge airfoil because a double-wedge generates more lift than biconvex airfoils in supersonic flow [7]. The geometry of both the nozzle and the vane profile is shown in Fig. 2.

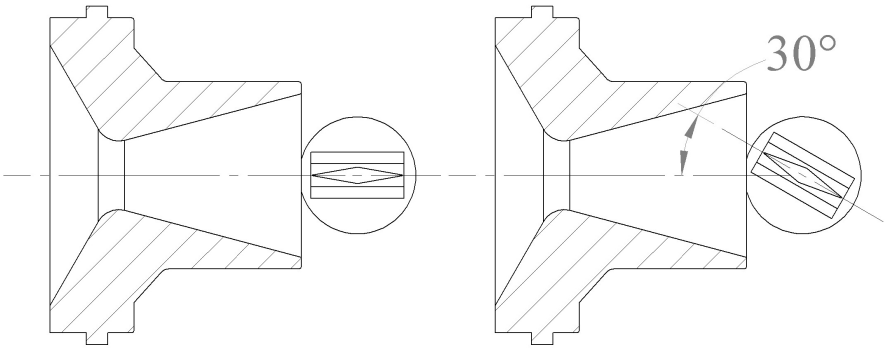

(a) 0 degree deflection. **(b) 30 degree deflection.**

Fig. 1 Examples of vane deflection with respect to motor's exhaust.

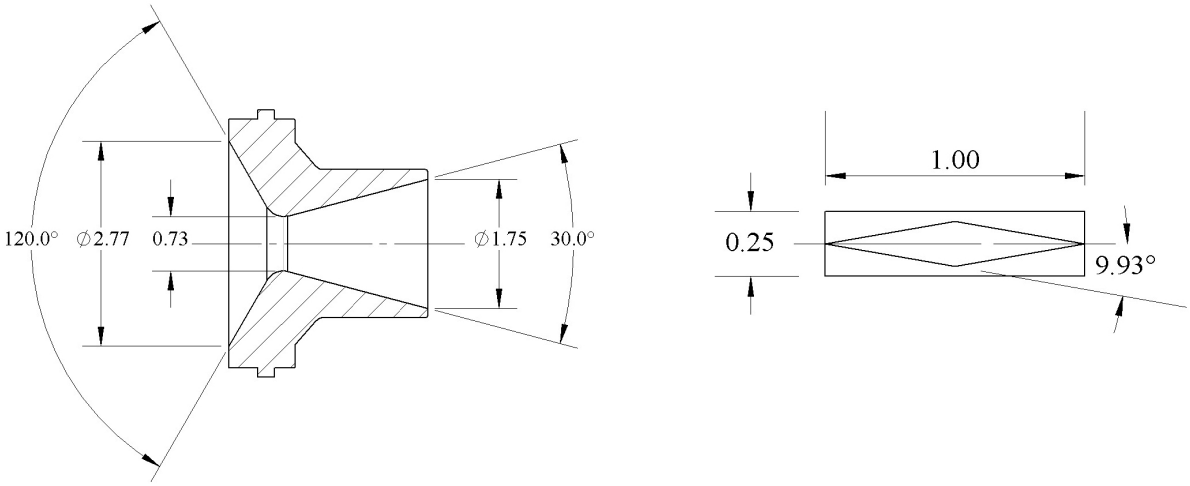

(a) RCS 98 mm nozzle geometry. **(b) Jet vane profile.**

Fig. 2 Geometry of the nozzle and vane modeled in this study (dimensions in inches) [8].

The complete JVTVC assembly, shown in Fig. 3a, is too mechanically complex to properly mesh and simulate without geometry simplifications. Thus, the side force characterization study used a defeatured assembly consisting of only the vanes and vane backings, which are the only components expected to generate significant aerodynamic forces. This simplified assembly can be seen in Fig. 3b. The CHT study also used a defeatured assembly consisting of vanes, vane backings, axles, and other servo-connecting components modeled as a single cylindrical component. More components were included in this study to understand the heating effects through a wider range of critical components. This assembly and its cross-section can be seen in Fig. 3c and Fig. 3d. Further simplifications were made in both assemblies by removing screws and holes to minimize the number of smaller cells required to mesh these complicated features.

Regarding the fluid region, the flow from the AeroTech N1000W-PS and RCS 98 mm nozzle is contained in a cylindrical volume with a 30 inch diameter and 60 inch length to accurately simulate atmospheric effects and minimize boundary interference. To ensure accurate placement of the jet vanes in relation to the motor's exhaust, a curve of the nozzle's exit was included. This extended the overall length of the nozzle by 0.03 inches while maintaining the same divergence angle of the nozzle. This change was assumed to be negligible because the flow is not expected to remain attached along this portion of the nozzle due to its high curvature. This change allowed the backings to remain in the fluid region and be fully included in the simulation. The symmetrical nature of each geometry was also used to minimize the total mesh cell count and simulation time. Since the side force study involved paired vane deflections, only half of the geometry was modeled; the symmetry condition was applied to accurately represent the complete configuration. The

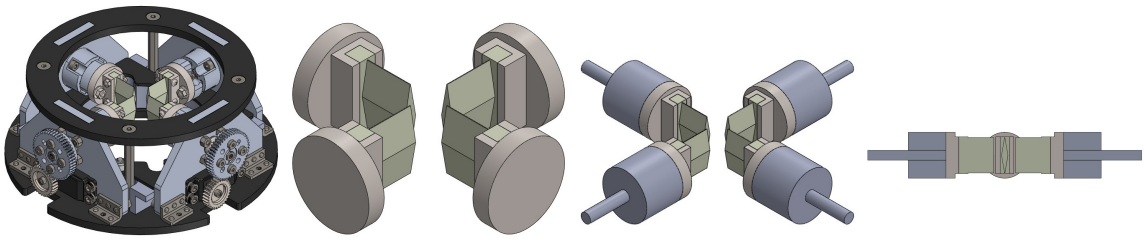

(a) Full vane assembly. **(b) Side force characterization assembly.** **(c) CHT analysis assembly.** **(d) Cross-section of CHT analysis assembly.**

Fig. 3 Full and simplified vane assemblies used in computational studies.

heating study did not consider any vane deflections, so a quarter geometry was modeled with two symmetry conditions. The final fluid domain used in both the side force and heating study is shown in Fig. 4a and Fig. 4b.

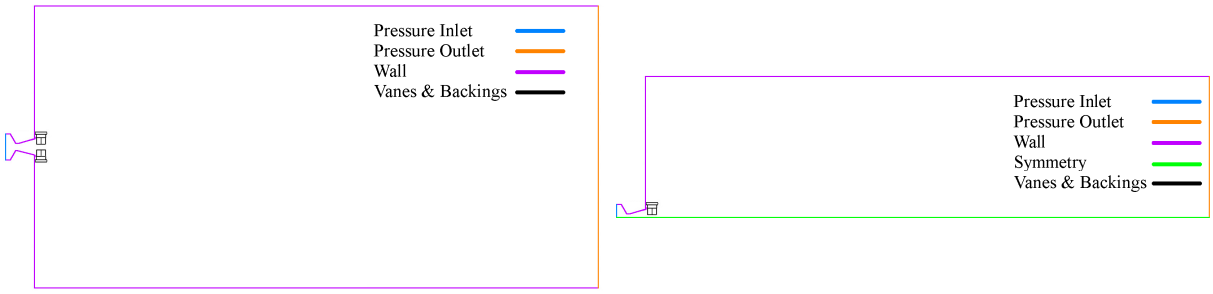

(a) The half geometry used for the side force characterization. **(b) The quarter geometry used for the CHT analysis.**

Fig. 4 Computational domains used in this study.

The full geometry was prepared in SolidWorks and the 3D domain was finalized in Ansys SpaceClaim. A 3D domain was required to capture the flow's transverse behavior over the vane assembly to produce accurate lift and drag information to characterize the vane's aerodynamic forces and heating behavior.

IV. Mesh Generation

Ansys Fluent meshing was used to generate an unstructured mesh for these computational geometries. Three main characteristics were considered throughout the meshing process: skewness, orthogonality, and cell count. These characteristics were used in defining the meshing parameters along with data from mesh convergence studies. Using these requirements, there was a focus on refining the cell size at the inlet, nozzle walls, vanes, and vane backings, regions of complex flow interaction. Inflation layers were also included along the nozzle walls, vane, and vane backings to avoid using wall functions. The inflation layers on the nozzle walls and front wall used a uniform specification, while the vane and vane backings used a smooth transition specification. A sufficiently refined inflation layer was defined to have a y+ value below 5 to remain in the viscous sublayer, otherwise boundary layer effects may be captured inaccurately [9]. A body of influence was also created around the vanes and backing to capture the flow behavior around these parts as well as in the wake and exhaust region. The quarter geometry and half geometry utilized similar meshing parameters, although the quarter geometry had a higher cell density due to the increased complexity of the geometry. The final cell counts for the half geometry and quarter geometry were around 5 million and 3 million cells, respectively. Additionally, the final maximum surface skewness was around 0.66 and the final minimum volumetric orthogonality was around 0.15.

V. Simulation Methods

The governing equations used to simulate this flow are conservation of mass, conservation of momentum, and conservation of energy. By assuming a Newtonian fluid and continuum flow, the Navier-Stokes equations can be derived. For this study, the Reynolds-Averaged Navier-Stokes (RANS) method was employed by time-averaging the Navier-Stokes equations into mean and fluctuating components. The RANS method sacrifices accuracy in favor of a more computationally efficient method to model turbulence compared to direct numerical simulation or large eddy simulation. However, solving the RANS equations requires the choice of a turbulence closure model to close the eddy viscosity term used to represent the Reynold's stresses [10].

A. Turbulence Modeling

Common eddy viscosity turbulence models in CFD include the two-equation $k-\epsilon$ and $k-\omega$ models, and the one-equation Spalart-Allmaras model. The flow of interest features a significant amount of shocks and flow separation. The $k-\epsilon$ model uses approximate wall functions to model near-wall flow rather than directly resolving this layer, causing it to perform poorly in flows with strong adverse pressure gradients [11]. The $k-\omega$ model, which uses the specific turbulence dissipation rate, has improved performance in these types of flows. However, this model is highly sensitive to freestream turbulence conditions, causing overprediction of wall shear stress [12]. The $k-\omega$ SST model improves upon this by combining the $k-\omega$ model near the wall and the $k-\epsilon$ model farther from the wall using a blending function. Another blending function is used as a viscosity limiter near the wall for better wall shear stress prediction. A more computationally efficient one-equation model known as the Spalart-Allmaras model has been shown to be effective at capturing external aerodynamics, but with less accuracy in regions of excessive flow separation [13, 14]. Ultimately, the $k-\omega$ SST model was used for its accuracy compared to the Spalart-Allmaras model.

B. Solver Settings

The strong coupling between the pressure and velocity terms of the governing equations was accounted for using a coupled algorithm, and a gradient computation was performed using the least squares cell-based method. Due to the skewed cells created in the unstructured mesh, the least-squares gradient method offers a similar level of accuracy as the Green-Gauss node-based gradient method. However, the increased computational efficiency of the least squares method made it more favorable. Finally, spatial discretization of flow variables was calculated using a second-order upwind scheme which shows stronger performance in unstructured meshes [9].

This study utilizes the steady-state density-based solver to handle the strong compressibility effects present in supersonic flow by coupling the solutions of the mass, momentum, and energy equations [9]. Transient simulations of the jet vanes at different thrust values and deflection angles are computationally expensive and generally infeasible. Furthermore, due to the supersonic nature of rocket nozzle exhaust, it was assumed that real-world convergence of the side force would occur in small timescales. Hence, a steady-state solution can be used to find the side force generated by a jet vane at an arbitrary deflection angle and chamber pressure.

To perform the CHT analysis in a computationally efficient manner, some changes were made to the procedure. First, a simulation using the quarter geometry yielded a converged steady-state solution of the flow around the jet vanes. Following this, the solver type was switched from steady density-based to transient pressure-based. Unlike the density-based solver, which solves the conservation of mass, momentum and energy together, the pressure-based solver decouples the conservation of energy equation [9]. With the energy equation decoupled from the mass and momentum equations, the transient solver was run solely for the energy equation. However, since this simulation was run after the steady-state solution, a patch re-initialized the solid regions to 298 K. Overall, solving the energy equation on its own decreased computational cost significantly since only one equation is being solved. In the case of transient modeling of fluid flow, a time step fulfilling a sufficiently small Courant number is recommended to prevent numerical instabilities. However, since heat diffusion was the main phenomenon being modeled, a larger time step was used. The size of the time step was increased to 0.01 seconds, and as a result, the entire 13.1-second simulation of the motor's burn was executed more efficiently [15].

C. Material Properties

The material properties for the solid and fluid cells were modeled using both the GRANTA MDS database and the Fluent database. Beginning with the solid cells, the vanes and backings were configured using data from the GRANTA MDS database. The vanes were simulated as *tungsten-pure-r07004*, and the backings were simulated as

titanium-alloy-ti-6al-4v-aged, which reflect the actual materials used. The specific properties of the vanes were set to have constant density, a piecewise-linear specific heat capacity, and piecewise linear thermal conductivity to account for the changes in these material properties with respect to temperature. The backings were set to have constant density, constant specific heat capacity, and constant thermal conductivity because it was not expected to undergo a large temperature change. The axle and other servo connecting components were configured using data from the Fluent database. The axle was simulated as *steel*, and the other connecting components were simulated as *aluminum*. Default values for the specific properties were used for both materials to remove complexity from the transient simulation and reduce computational time.

The fluid cells of the domain were configured to represent the motor's exhaust as accurately as possible as a single fluid rather than a mix of species. Species mixing could provide more accurate results, but specific data regarding the motor's exhaust and particles were not available. Many fluid properties were found from the AeroTech N1000W-PS propellant data sheet, though some were based off air due to insufficient propellant data [16]. The assumption of a constant molecular weight of 27.661 g/mol was made despite its potential inaccuracy due to molecular dissociation at high temperatures causing changes in its molecular weight. A polynomial function for the fluid's specific heat capacity was also created from the three available data points. Finally, an ideal gas density was also assumed as well as kinetic theory to find the thermal conductivity and viscosity of the air.

D. Boundary Conditions

The inlet boundary condition was configured to best represent the conditions within the solid rocket motor's chamber, so a pressure inlet specification was used. The momentum specifications of the pressure inlet include the stagnation pressure, static pressure, turbulent intensity, and turbulent viscosity ratio. The default values of 5% and 10 for turbulent intensity and turbulent viscosity ratio were used given their high accuracy in defining turbulent properties for internal flows [18]. The inlet static pressure was chosen using isentropic relations and the rocket thrust equations to sufficiently profile the thrust curve of the chosen solid rocket motor. The thrust curve of the AeroTech N1000W is shown in Fig. 5.

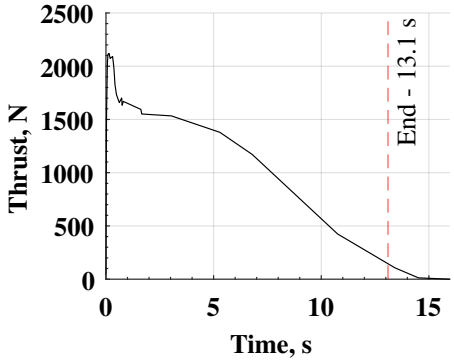

Fig. 5 The thrust curve of the AeroTech N1000W solid rocket motor used for this study ([17]).

Prior to solving for the thrust, some assumptions regarding the propellant data and the solid rocket motor were made to simplify analysis. First, the static temperature and static pressure in the combustion chamber were assumed to be the same at the nozzle inlet. Second, the specific heat ratio and molecular weight of the exhaust gas were assumed to be constant through the nozzle and flow domain. Additionally, the static temperature was assumed to be constant throughout the burn [19]. Finally, these equations also assumed isentropic flow, meaning stagnation properties were constant across the nozzle. The exhaust gas properties of the AeroTech N1000W were found using the propellant data sheet for *Slow White Lightning* which are summarized in Table 1.

Table 1 Summary of relevant fluid data for *Slow White Lightning* propellant used in the AeroTech N1000 W [16].

Property	Value
Chamber Static Temperature	2364.133 K
Specific Heat Ratio	1.245
Molecular Weight	27.661 g/mol
Specific Gas Constant	300.5676 J/(kg-K)

$$\dot{m} = \frac{A^* p_o}{\sqrt{T_o}} \sqrt{\frac{\gamma}{R}} \left(\frac{\gamma+1}{2} \right)^{-\frac{\gamma+1}{2(\gamma-1)}} \quad (1)$$

$$\frac{A}{A^*} = \left(\frac{\gamma+1}{2} \right)^{-\frac{\gamma+1}{2(\gamma-1)}} \frac{\left(1 + \frac{\gamma-1}{2} M^2 \right)^{\frac{\gamma+1}{2(\gamma-1)}}}{M} \quad (2)$$

$$v = M\sqrt{\gamma R T} \quad (3)$$

$$\frac{p}{p_o} = \left(1 + \frac{\gamma-1}{2} M^2 \right)^{-\frac{\gamma}{\gamma-1}} \quad (4)$$

$$\frac{T}{T_o} = \left(1 + \frac{\gamma-1}{2} M^2 \right)^{-1} \quad (5)$$

$$F_T = \dot{m} v_e + (p_e - p_a) A_e \quad (6)$$

Following these assumptions regarding the propellant data, the thrust could now be solved for given any input static pressure using the rocket thrust equations and isentropic relations shown in Eqs.(1) - (6) [20]. To adequately test a large range of the thrust curve, a wide range of inlet static pressures were used. These static pressures and their corresponding thrusts are displayed in Table 2. The static temperature was defined as 2364.133 K for all six input conditions.

Table 2 Summary of the conditions used for the pressure inlet.

Input Parameter	Condition 1	Condition 2	Condition 3	Condition 4	Condition 5	Condition 6
Static Pressure, MPa	4.8055	3.7923	3.1028	2.4133	1.7238	1.0343
Stagnation Pressure, MPa	4.8106	3.7963	3.1060	2.4158	1.7256	1.0353
Corresponding Thrust, N	2005.7937	1549.7144	1239.3599	929.0054	618.6509	308.2965

The outlet boundary condition was set to standard sea level conditions for comparison with future static fire data. Therefore, the gauge pressure was set to 101325 Pa and the temperature was set to 298 K.

VI. Results and Discussion

These presented CFD studies produced estimates for the side force generated by the vane and the thrust reduction due to the vanes and backings impeding the flow at varying deflection angles and chamber pressures. The final values generated were found by doubling the results from the half-geometry to account for the symmetry condition. This would reflect two vanes deflecting in the same direction on opposite sides. The total side force generated by the deflection of two vanes is displayed in Table 3. The side force was calculated by finding the lift on the deflected vanes. The amount of drag on all four vanes and vane backings is shown in Table 4. This drag is equivalent to the reduction in thrust caused by the vanes and backings impeding the flow.

Table 3 Simulated Side Force of All Deflected Vanes, N

Deflection, Deg	Condition 1	Condition 2	Condition 3	Condition 4	Condition 5	Condition 6
0	0.4028	0.2202	-0.2862	-0.2426	0.0934	0.1912
10	100.7640	78.4146	59.7170	41.2428	25.1500	8.3294
20	188.0932	144.6400	112.4574	79.6836	48.5228	20.9302
30	260.4536	200.4914	154.8882	110.3580	70.1722	34.3394

Table 4 Simulated Total Thrust Reduction of All Vanes, N

Deflection, Deg	Condition 1	Condition 2	Condition 3	Condition 4	Condition 5	Condition 6
0	60.6811	48.2319	39.4310	31.5019	21.2560	13.6282
10	82.0036	63.1136	51.0052	38.1428	25.0867	15.4436
20	139.9528	107.0449	85.4405	63.1938	39.0554	23.2552
30	234.7305	180.4000	142.9150	103.9787	62.4505	40.6558

During these simulations, as the chamber pressure decreased, a significant degree of overexpansion was observed. This is reflected in Fig. 6, and this phenomenon was especially prevalent with the 1.0 MPa chamber pressure or condition 6 (Fig. 6c). At such low chamber pressures, the static pressure at the nozzle exit plane is very small, causing major flow separation.

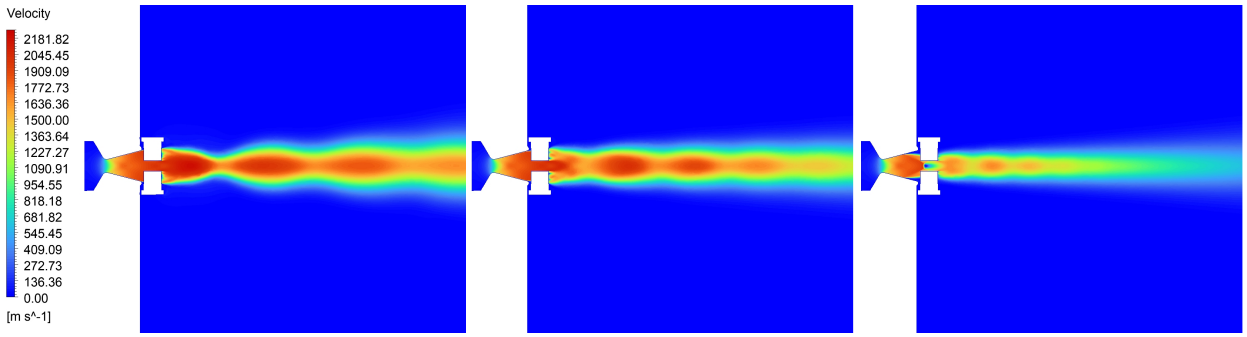

(a) Condition 1. **(b) Condition 4.** **(c) Condition 6.**

Fig. 6 Velocity contours for all chamber pressures at a 0 degree deflection angle.

As a result of the significant overexpansion and flow separation, the thrust values computed by the rocket thrust equations are inaccurate [21]. Therefore, an iso-clip was created in Fluent to generate a circular plane at the nozzle exit. Area-weighted average values of pressure, velocity and mass flow rate were obtained at this plane to calculate thrust with Eq. 6. The Fluent-calculated thrust and the thrust derived by the isentropic rocket equations are compared in Table 5.

Table 5 Thrust comparison between isentropic calculations and Fluent obtained values.

Thrust, N	Condition 1	Condition 2	Condition 3	Condition 4	Condition 5	Condition 6
Isentropic	2005.7937	1549.7144	1239.3599	929.0054	618.6509	308.2965
Fluent-calculated	1881.0915	1451.9306	1149.4051	839.6658	494.6132	169.2181
Percent Difference, %	6.6292	6.7347	7.8262	10.6399	25.0777	82.1889

Examining the velocity contours at other vane deflections also validates the potential of the jet vanes to manipulate the thrust vector. The vectored thrust as the vanes are deflected can be seen in the velocity contours of Fig. 7.

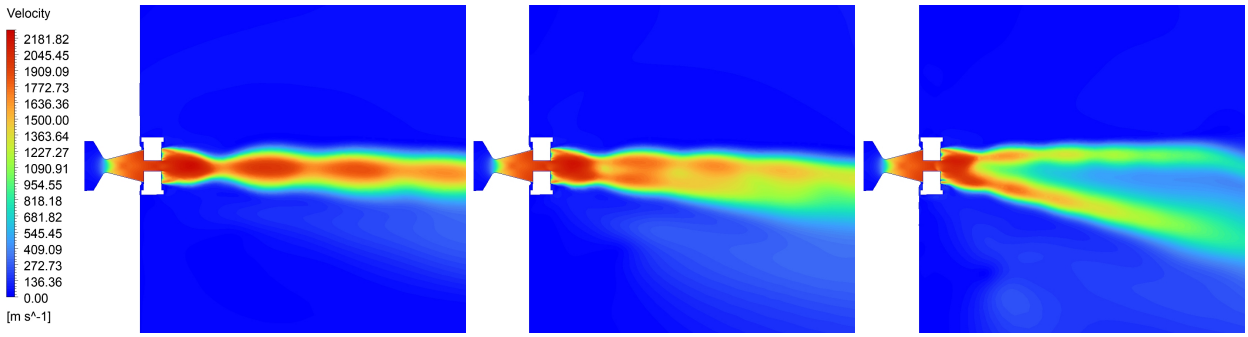

(a) 10° **deflection angle.** **(b)** 20° **deflection angle.** **(c)** 30° **deflection angle.**

Fig. 7 Velocity contours of condition 1 for deflection angles of 10 to 30 degrees.

To interpolate and extrapolate results for untested conditions, a regression model was developed. Two equations were created: one to return the side force as a percent of thrust as a function of the deflection angle, and another to return the thrust reduction as a percent of thrust as a function of deflection angle and thrust. These equations would only be applied to regions of the thrust curve in Fig. 5 with similar conditions to what was simulated. Specifically, these equations would be used for the thrust domain between 2 - 12 seconds.

The first step in developing a regression model was to clean the data set. Beginning with the side force and drag output data, these sets were normalized by the Fluent-calculated thrust. Additionally, due to the significant flow separation experienced at the 1.0 MPa input condition, these points were excluded from the regression model. Moreover, when the chamber pressure is this low, the thrust is small and would not be included within the range of thrusts necessary for the regression model. Instead of using the chamber pressure as an input, the Fluent-calculated thrust was used instead. Furthermore, the deflection angle was left as an input in degrees. The second step in solving the regression problem is determining which features should be included. A simple approach is to plot the side force and thrust reduction data against the deflection angles and the thrust input to identify which features are the most influential. Shown in Fig. 8, the side force was determined to be linear with the deflection angle and constant with thrust. Using Fig. 9, the total drag was determined to be quadratic with the deflection angle, linear with thrust, and have a nonzero y-intercept. A problem encountered in linear regression is overfitting, which can occur when an excess of features results in the model fitting to the noise and error of the data rather than the true trend. Therefore, to prevent overfitting to the small error in CFD, no other features were added. The third and final step in solving the regression problem is utilizing a method for finding the most optimal parameters. For the purposes of simplicity, a least squares approach was used to solve for the optimal parameters. Utilizing the least squares fit, the values for the regression model were determined as shown in Equations (7) and (8). The mean absolute error was then calculated between the regression model and the simulated results to assess the accuracy. The final MAE for the side force model was 0.33% and the final MAE for the thrust reduction model was 0.14%.

$$F_{\text{Side Force}} = E\alpha, E = 4.7060 \times 10^{-3} \tag{7}$$

$$F_{\text{Thrust Reduction}} = B + CF_{\text{Thrust}} + D\alpha^2, B = 4.051 \times 10^{-2}, C = 9.8673 \times 10^{-5}, D = -3.9928 \times 10^{-6} \tag{8}$$

The data from the simulations was plotted to compare with the outputs of the regression models in Fig. 8 and Fig. 9. With an accurate model in place, applications towards designing a JVTVC system can now be created. In particular, these regression equations allow for calculation of vane forces without running extremely computationally expensive simulations, which is critical for real-time flight control. For example, using this model, a controller could be designed considering how different vane deflection angles will affect the orientation and position of the rocket. Simulations for the rocket's flight can validate if active stabilization can be achieved in various atmospheric conditions, such as high or low cross-winds or just general system validation when running Monte Carlo simulations.

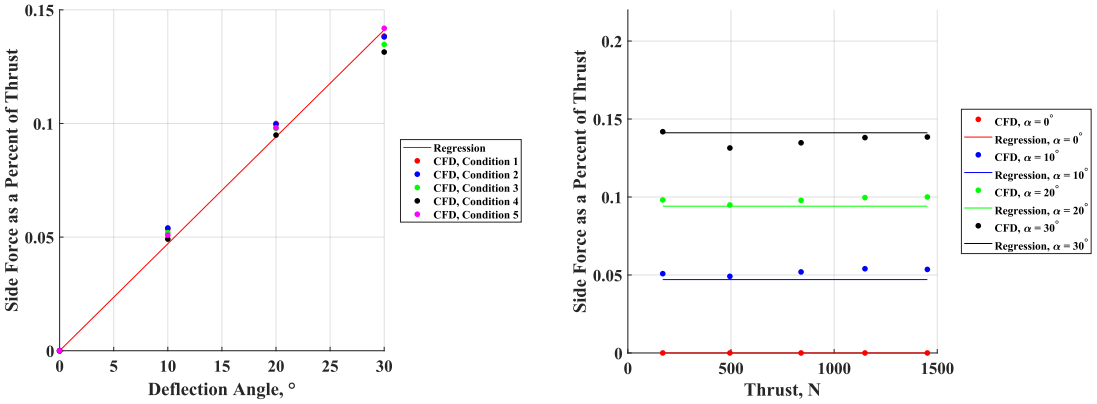

(a) As a function of the deflection angle. **(b) As a function of the thrust input.**

Fig. 8 The side force as a percent of thrust shown as functions of the deflection angle and thrust.

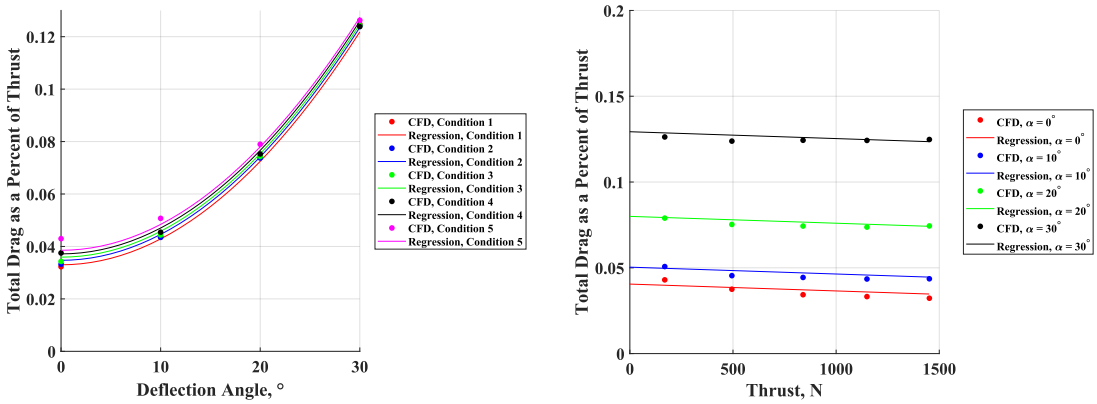

(a) As a function of the deflection angle. **(b) As a function of the thrust input.**

Fig. 9 The total drag as a percent of thrust shown as functions of the deflection angle and thrust.

Table 6 Maximum temperature of JVTVC components at 13.1 s.

Component	Temperature, K
Axle	349.132
Other Components	326.723
Backing	1369.560
Vane	1946.830

Fig. 10 shows the evolution of temperature within the vane assembly over time to reflect the rocket motor's burn. These contours were generated through the preliminary transient CHT analysis, where the flow and solid regions are thermally coupled. This visualization demonstrates how heat from the rocket exhaust is conducted through the vanes and their supporting structures over time. With this information, it is possible to assess material performance, identify potential hot spots, and verify that the vane assembly can withstand the thermal loads during the motor's burn. The maximum temperatures of each component at the end of the motor's burn can be seen in Table 6. These maximum temperatures validate that no specific components experience localized melting [22].

Ultimately, the transient temperature profile helps guide the selection of vane and backing materials, the design of any required cooling strategies, and the establishment of safe operating limits. Furthermore, this method of performing transient CHT simulations provides a much more computationally efficient process in comparison to a complete transient CHT simulation.

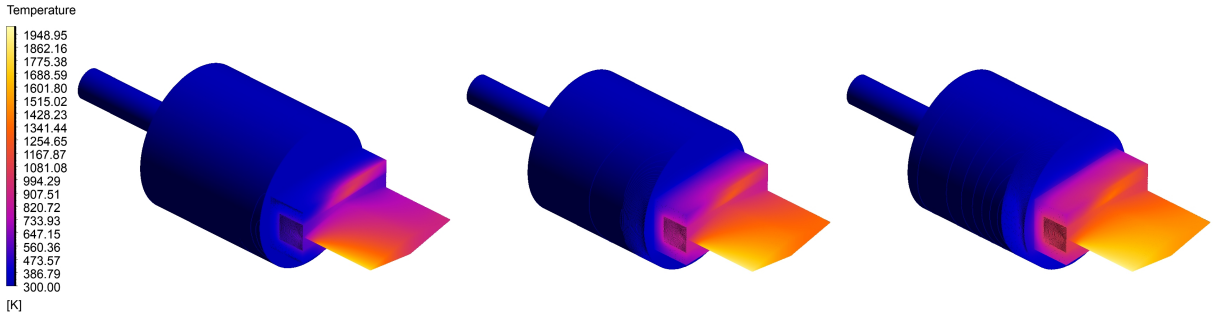

(a) $t = 2$ **s** **(b)** $t = 6$ **s** **(c)** $t = 13$ **s**

Fig. 10 Temperature of JVTVC components through motor's burn time.

VII. Conclusion

3-D CFD analyses were performed to computationally model jet vanes for thrust vector control to guide and validate the design of a JVTVC system. Steady-state simulations of a simplified JVTVC assembly consisting of jet vanes and vane backings produced side force and thrust reduction data characterizing the vanes' performance. Based on the sampled data, a least-squares regression was employed to derive functions that relate deflection angle and thrust to the side force and thrust reduction at varying input conditions. These regression models allow for accurate interpolation and extrapolation of the vane forces despite the limited sample size of this study. These results, validated by visual

velocity contours, confirm the potential of the JVTVC system to vector thrust. A transient CHT analysis of another simplified JVTVC assembly consisting of jet vanes, vane backings, axles, and other servo connecting components was also conducted. The results of this transient method are preliminary analyses that produced an evolution of the vane assembly's temperature over the motor's burn time. The contours from this data showed potential hot spots on the vane's edge and also validated that the chosen materials can withstand the thermal loads they will experience while in use. These methods presented can help guide the computational modeling of jet vanes for thrust control in designing rockets with active stabilization.

Acknowledgments

This work was supported by the Georgia Tech Guggenheim School of Aerospace Engineering. Special thanks is given to Ansys, Inc. for providing the software used in this study.

References

[1] Lloyd, R., and Thorp, G., "A review of thrust vector control systems for tactical missiles," *14th Joint Propulsion Conference*, 1978, p. 1071.

[2] Shandor, M., Stone, A., and Walker, R., "Secondary gas injection thrust," , 2019.

[3] Sung, H.-G., and Hwang, Y.-S., "Thrust-vector characteristics of jet vanes arranged in x-formation within a shroud," *Journal of Propulsion and Power*, Vol. 20, No. 3, 2004, pp. 501–508.

[4] Thakre, P., and Yang, V., "Chemical erosion of refractory-metal nozzle inserts in solid-propellant rocket motors," *Journal of Propulsion and Power*, Vol. 25, No. 1, 2009, pp. 40–50.

[5] Zeamer, R. J., "Liquid-Injection Thrust Vector Control." *Journal of Spacecraft and Rockets*, Vol. 14, No. 6, 1977, pp. 321–322.

[6] Murty, M., and Chakraborty, D., "Numerical characterisation of jet-vane based thrust vector control systems," *Defence Science Journal*, Vol. 65, No. 4, 2015, pp. 261–264.

[7] Zulkarna-En, M., ISLAM, M. A., Al Faruk, A., Islam, M. R., and Mukut, A. N. M. M., "Numerical Analysis of Aerodynamic and Shock Wave Characteristics of Biconvex and Double-Wedge Shape Airfoils for Supersonic Flow," *International Journal of Automotive and Mechanical Engineering*, Vol. 20, 2023, pp. 10821–10837. https://doi.org/10.15282/ijame.20.4.2023.02.0837.

[8] Components, R. R. M., "98mm Nozzle 0.734" Throat Summary," https://www.rocketmotorparts.com/product/98mm-nozzle-0-734%22-throat, 2025.

[9] ANSYS, "ANSYS FLUENT 12.0 Theory Guide," *ANSYS FLUENT 12.0/12.1 Documentation*, 2024.

[10] Hinze, J., *Turbulence*, McGraw-Hill, 1975.

[11] Apsley, D., and Leschziner, M., "Advanced turbulence modelling of separated flow in a diffuser," *Flow, turbulence and combustion*, Vol. 63, 2000, pp. 81–112. https://doi.org/https://doi.org/10.1023/A:1009930107544.

[12] Greenshields, C., and Weller, H., "Notes on Computational Fluid Dynamics: General Principles," , 2022. Accessed: 2025-03-02.

[13] Tong, O., *Verification and validation of the Spalart-Allmaras turbulence model for strand grids*, Utah State University, 2013.

[14] Spalart, P., and Allmaras, S., "A One-Equation Turbulence Model for Aerodynamic Flows," *AIAA Journal*, Vol. 30, No. 5, 1992, pp. 876–884. https://doi.org/10.2514/6.1992-439.

[15] Richards, K. J., Senecal, P. K., and Pomraning, "Conjugate Heat Transfer: Benefits and Capabilities," https://convergecfd.com/benefits/conjugate-heat-transfer, 2025. Accessed: March 2, 2025.

[16] Components, R. R. M., "98mm Slow White Lightning™ Propellant Grain Summary," https://www.rocketmotorparts.com/98mm_Slow_White_Lightning__Propellant_Grain/p1577809_20931771.aspx, 2025.

[17] Coker, J., https://www.thrustcurve.org/motors/AeroTech/N1000W/, April 2009.

[18] ANSYS, "ANSYS FLUENT 12.0 User's Guide," *ANSYS FLUENT 12.0/12.1 Documentation*, 2024.

[19] Seidel, H., "Transient chamber pressure and thrust in solid rocket motors," *Prepared for Advanced Systems Laboratory, R&D Directorate, US Army Missile Command, Technical Note R-138*, 1965.

[20] Center, G. R., "Rocket Thrust Summary," https://www.grc.nasa.gov/www/k-12/airplane/isentrop.html, 2021.

[21] Sutton, G. P., and Biblarz, O., *Rocket propulsion elements*, John Wiley & Sons, 2011.

[22] Bauccio, M. E., *ASM Engineered Materials Reference Book*, 2nd ed., ASM International, Materials Park, OH, 1994.